MICROROBOTS

Floating magnetic microrobots for fiber functionalization

Antoine Barbot[1]*, Haijie Tan[1]*, Maura Power[1], Florent Seichepine[1], Guang-Zhong Yang[1,2]†

Because minimally invasive surgery is increasingly used to target small lesions, demand is growing for miniaturized tools—such as microcatheters, articulated microforceps, or tweezers—that incorporate sensing and actuation for precision surgery. Although existing microfabrication techniques have addressed the construction of these devices, accurate integration and functionalization of chemical and physical sensors represent major challenges. This paper presents a microrobotic platform for the functionalization of fibers of diameters from 140 to 830 micrometers, with a patterning precision of 5 micrometers and an orientation error below 0.4°. To achieve this, we developed two 2 millimeter–by–3 millimeter, 200-micrometer-thick microrobots to align floating electronic circuits on a fiber during a wet transfer process. The position and orientation of the microrobots were controlled at the air/water interface by a permanent magnet. The stiffness of the position controlled was 0.2 newton millimeter, leading to an average force of 0.5 newton. The nonhomogeneous magnetic field of the magnet, associated with different preferred magnetization directions recorded in the microrobots, allowed the distance between the two microrobots to be precisely controlled. This extra degree of freedom was used to control the microrobot pair as a tweezer to grab and release floating electronic patterns, whereas the others were used to align the pattern position and orientation with the fiber. A model of this control, as well as the microrobots' interaction through surface tension, is proposed. Detailed performance validation is provided, and various exemplar sensor embodiments on a 200-micrometer-diameter fiber and three-dimensional devices are demonstrated.

INTRODUCTION

With increasing clinical emphases on improved surveillance and earlier diagnosis, the future of surgery is moving toward precision intervention, which demands improvements to the access and the accuracy of current minimally invasive techniques. Although large-scale robotic platforms are gaining clinical acceptance, the future of medical robotics is shifting toward endoluminal and transluminal access with smart, articulated microinstruments for managing early malignancies guided by in situ, in vivo imaging and sensing. Recent introduction of robotic tools integrated on fiber (fibrebot) has allowed the integration of imaging, sensing, and micromanipulation, all in a single fiber. Sophisticated microgrippers have already been directly fabricated on the tip of a fiber with two-photon polymerization (*1*). Microactuation can be enabled through hydraulic links by leveraging microcapillary function (*2*), and the device could be further used for targeted drug delivery and focused energy, e.g., CO_2 laser ablation.

Optical fibers represent a versatile substrate for developing such flexible microtools. Their surface further provides an ideal location to integrate multiple sensors along its length. However, direct patterning of microelectronics onto small, curved objects is challenging because existing microfabrication processes are primarily tailored to flat substrates. Transfer methods, with which devices are first fabricated onto flat silicon chips and subsequently picked up and transferred onto the target substrate, are commonly used to embed miniaturized electronics onto curvilinear [and other three-dimensional (3D)] structures. Such techniques also allow the transfer of 2D crystals (e.g., graphene and MoS_2) from the growth substrate to an arbitrary substrate or device.

To date, two main transfer methods have been developed. They are the dry transfer method, which typically uses thermal release tapes (*3*, *4*) or viscoelastic stamps (*5*, *6*) to execute the transfer, and the wet transfer method (*7*–*12*), which involves wet etching of an initial substrate and subsequent mechanical scooping of a floating device film on the fluid surface using a target substrate. In general, dry transfer offers better cleanliness and higher precision over wet transfer, due to the absence of wet etchant and fluid or flow perturbation (*5*, *13*). Another challenge faced by wet transfer is that accurate positioning and scooping of the floating device is difficult, and there is a lack of precision tools or robotic platforms for such an approach. High precision in transfer and a controlled orientation of the stacked material are desirable for the study and fabrication of heterostructured devices based on 2D crystals (*14*).

In practice, the stamping approach used in dry transfer can be a challenge for the transfer of devices that wrap around 3D shapes, e.g., where site-specific force-sensing devices are required to wrap around a catheter. In such cases, the wet transfer approach can offer better pattern-to-substrate conformability by mechanically scooping the free-floating device film from underneath, allowing the film to wrap around and conform to the microtool (*15*–*17*). Despite having this advantage, wet transfer still faces the drawback of low precision due to the surface tension forces that dominate the air/water interface where the transfer occurs.

Using microrobot manipulators can address some of the major issues faced by manual wet transfer methods. Precise control is needed on the position of a floating pattern on the surface of a liquid medium and also on its rotation with respect to the surface normal of the liquid. Manipulation methods for such a task need to be capable of moving the pattern over a surface area of several square centimeters and in submicrometer precision to make successive layers of a device or to align the devices with a preexisting 3D structure. Commercial piezoelectric stages or arms may be used, but such systems may not be easily adapted for them to work at the water interface

---

[1]Hamlyn Centre, Imperial College London, London, UK. [2]Institute of Medical Robotics, Shanghai Jiao Tong University, Shanghai, China.
*These authors contributed equally to this work.
†Corresponding author. Email: g.z.yang@imperial.ac.uk, gzyang@sjtu.edu.cn

without creating disturbances due to surface deformation. Here, we propose the use of mobile microrobots at the air/water interface to allow for precise control of the pattern movement, naturally restrained on a 2D plane even if it is deformed, whereas the lateral friction (mostly due to the surface drag of water) is minimized and smooth. Moreover, untethered manipulation induced minimal interaction with the water surface, which avoids perturbation.

In considering the possible embodiments of such smaller and untethered alternatives, studies have revealed a range of different microrobot manipulators that operate in liquid environments that could be adapted for this application. For example, using optical trapping, light can be used to precisely control the position and orientation of microrobots in a 2D plane of a liquid environment. However, optical tweezers are only capable of producing forces in the piconewton range and are therefore unsuitable for moving floating films for electronic patterning. Larger forces can be generated using magnetic steering, which has been demonstrated to directly push a target object (*18*) in a liquid environment or to indirectly manipulate objects by inducing local flow (*19*). In a similar manner, other types of swimming robots could be used to push a floating pattern such as catalytic microrockets (*20*) and surfaces with acoustically excited microcavities (*21*), both of which use locally generated microbubbles for thrust. To achieve better precision and control than simply pushing an object at just one contact point, multiple microbots can be used at various points around an object in a cage formation (*22*). Different examples of floating microrobots have already been proposed using various propulsion and control mechanisms such as magnetic gradient (*23*) and laser actuation (*24*). Recently, mechanisms to trap objects with magnetic microrobots at the water surface have been proposed either by spinning to trap the particle on an orbit (*25*) or by tilting the robot to create an attractive force from the deformation of the air/water interface (*26*). Our method combines the precision and range of a conventional stage with tailored design magnetic microrobots that are specifically suited to the task of manipulating a floating patterned film. To enable simple yet precise control, we propose a pair of floating microrobots for grasping the floating pattern on both sides. This was achieved by using a nonuniform magnetic field generated by a single permanent magnet combined with tuning of the magnetization direction of the robots' constituent material. The interaction between the microrobots and the magnetic field allowed the microrobot pair to be positioned at two different locations at the air/water interface when placed under the magnet, thus forming a gripper (Fig. 1).

Instead of storing a permanent magnetization direction (*27*, *28*), we have stored only a preference for magnetization direction. Therefore, the microrobots did not store any magnetization when no magnetic field was applied. They were designed, rather, to magnetize in a particular direction when placed under the control magnet. To achieve this, we have cured an elastomer mixed with iron powder under a specific weak magnetic field generated by the permanent magnet used for subsequent control. This allowed the iron powder to be fixed in a specific direction as shown in Fig. 2A.

The relative horizontal translation and the rotation of the magnet controlled the translation and the rotation, respectively, of the coupled floating robot pair. The distance between the two microrobots was controlled by the distance between the magnet and the microrobot, as shown in Fig. 2B. Thus, these four degrees of freedom (DOFs) allowed for control over grasping (one DOF), position (two DOFs), and orientation (one DOF) of the pattern for the wet transfer onto the fiber.

The microrobot pair could perform pattern transfer onto a fiber with a high accuracy (5 μm and 0.4° precision) as well as near-full coverage of the fiber circumference (about 320°). This approach, therefore, addresses one of the key deficiencies of the wet transfer method (i.e., the lack of precision) and offers a promising route for fabricating miniaturized devices onto surgical microtools.

RESULTS

Magnetic microrobot gripper

With most magnetically controlled swimming microrobots, each microrobot of a given experiment is magnetized in a similar way, and therefore, they react in the same manner for a given magnetic field. However, for secure grasping, the individual microrobots need to react differently to the same magnetic field. Therefore, magnetic microrobots with different preferred magnetization directions were used so that they could move relatively to one another within the workspace. To achieve this, we used an elastomer, polydimethylsiloxane (PDMS), mixed with iron powder. A 200-μm layer of the mixture was then placed under a nonhomogeneous magnetic field created by a distant magnet as shown in the schematic in Fig. 3A. The weak magnetic field (between 12 and 7 mT) led to the assembly of iron lines after the direction of the magnet's own magnetic field, as shown in Fig. 2A. The PDMS was then thermally cured, thus physically keeping the iron line structure in place and fixing their orientation. For iron concentration from 10 to 40%, no stress-induced deformation was observed in the film after curing. Because the magnetic field applied is inhomogeneous, the directions of the lines vary throughout the composite polymer layer for different positions on the x-y plane. Although the y axis (perpendicular to the south-north magnet axis) has a negligible impact on the vertical component of magnetization (as shown in Supplementary Material A), the variation along the x axis (in the direction of the south-north magnet axis) dominates. To quantify this effect, we performed x-ray microtomography (Bruker MicroCT Skyscanner 1272) on the cured polymer matrix along its x direction for a 60 mm–by–2 mm width band. The iron lines' orientations along the x axis were then measured on reconstructed slices such as the one shown in Fig. 3A. Systematic measurements of the orientation of the iron powder lines have been performed (*29*). As presented in Fig. 3B, the angle of the iron line orientation followed the one of the magnetic field generated by the permanent magnet. In the central region, where the magnetic field gradient was the highest, a higher concentration of iron particles near the surface prevented the formation of visible oriented iron lines on the z/x plane.

The different regions of the iron/PDMS layer fabricated via this method correspond to different preferable directions of magnetization of the material. As a result, pairs of microrobots with different preferred magnetization directions could be made by using different parts of the iron/PDMS layer. To this end, the layer was stamped using a metal grid cutter (as presented in Supplementary Material B) to form rectangular robots that measure 2 mm by 3 mm and are 200 μm thick. In addition, small tooth-like structures were added to the microrobot design. This tooth structure ensured minimal surface tension interaction between the microrobot and the pattern to be transferred because only contact points were made. Therefore, it limited the movement of the pattern during the grasping process. The pattern tended to slide away when square microrobots were used for grasping. The surface deformation for both cases is visualized in Supplementary Material B. For characterization, when no gripping

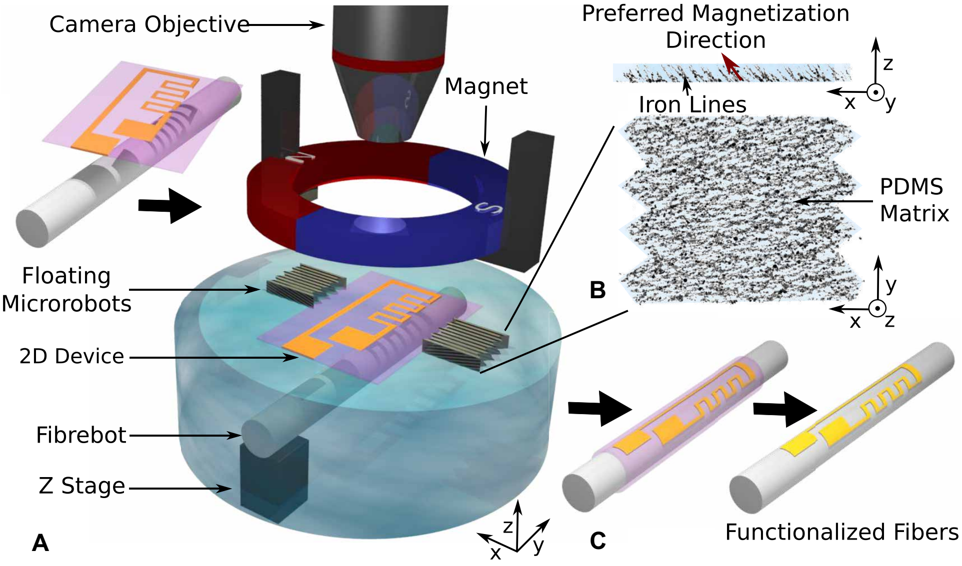

Fig. 1. Setup of the microrobot-assisted high-precision wet transfer. (**A**) Magnetically controlled microrobots via an external magnet to align a floating 2D device on a target substrate (e.g., optical fiber and 3D microdevice). (**B**) View of the microrobot structure in which iron lines trapped in an elastomer matrix are used to store a preferred magnetization direction. (**C**) Final assembled devices featuring the functional pattern aligned with a 5-μm and 0.4° precision.

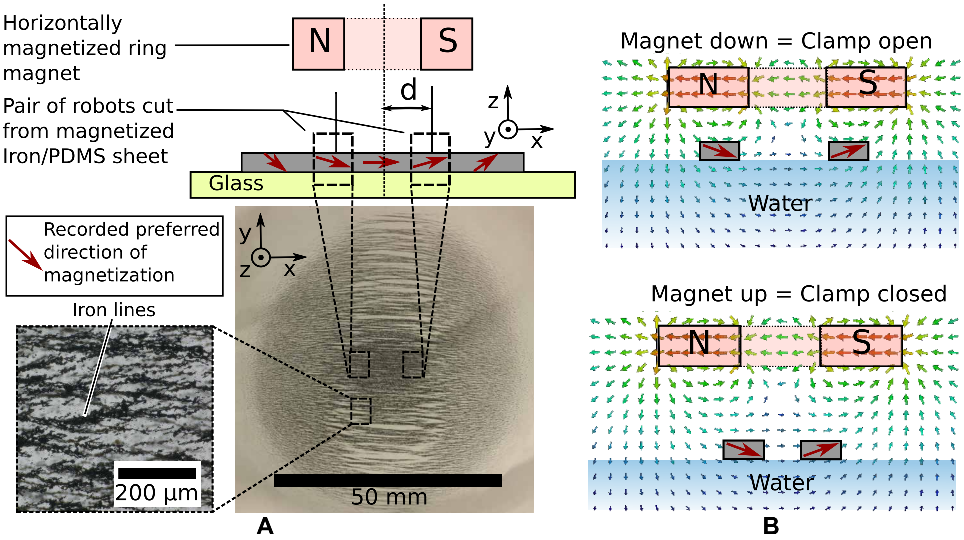

Fig. 2. Floating microrobots with different preferred magnetization directions: Fabrication and control principles. (**A**) Fabrication of microrobots. Different magnetization directions were programmed in the material with a ring magnet. (**B**) Clamping mechanism used in this study. Microrobots were moved together or apart depending on the vertical position of the magnet, allowing effective clamping of the pattern to be transferred, followed by rotational and orientation control.

was required, the microrobots were simply cut in squares of 2 mm by 2 mm.

To characterize the microrobot with different preferred magnetization directions, we used the angle made between their magnetization and the horizontal plane. We assumed this magnetization to be aligned with the iron lines. We refer to this angle as α, as defined in Fig. 3A. Positive values of α lie in the north side of the magnet and correspond to a preferred magnetization direction facing up (toward the magnet); negative α values lie in the south and correspond to a preferred magnetization direction facing down (away from the magnet).

The positions of different microrobot pairs and their respective response to different vertical positions of the magnet are shown in Fig. 4A (i.e., with opposite α values). For those robots, the iron concentration in the matrix was 20%.

As the α value increased, so did the component of the vertical magnetization; thus, the equilibrium distance of the microrobots to the projected center of the magnet on the water surface also increased. This led to an increase in the distance between two microrobots with opposite α values. This change gave us an extra DOF to grasp the floating object between the two microrobots. For each microrobot pair, this distance was large when the magnet was close to the surface (minimum of 12 mm in this study) and reduced rapidly as the magnet traveled upward and away from the microrobots. As a result, two motion patterns were possible for the microrobot pairs depending on |α|. For microrobot pairs with |α| ≤ 20°, the two microrobots could snap together and needed to be detached manually. This effect, hereafter referred to as snapping, is due to capillary effects that overcome the equilibrium from the magnetic field (*30*). For microrobot pairs with |α| ≥ 20°, the distance between the microrobot reached a minimum before increasing again with the magnet height. In both snapping and nonsnapping cases, the height of the magnet could be used to control the distance between the two robots, thus regulating the opening and closing of the gripper formed by the microrobots. Note that flat robots could ensure a constant wet area on the microrobot. This is essential to prevent hysteresis in the opening and closing of the microrobot pair gripper as shown in Supplementary Material C.

To confirm that the gripping effect of the microrobot pair is caused primarily by the induced magnetization of the ferromagnetic microrobot by the magnet, we performed detailed modeling on the microrobot equilibrium. Figure 4B displays the simulated equilibrium points of different microrobot pairs depending on the height of the magnet. These results demonstrate the gripper spacing in response to the height of the magnet. This confirms that the equilibrium distance is mainly governed by the preferred magnetization direction α. However, the height at which the gripper pair opened in simulation is lower than that of the experimental results. This is attributed to the difference between the real and simulated magnetic fields, as demonstrated in

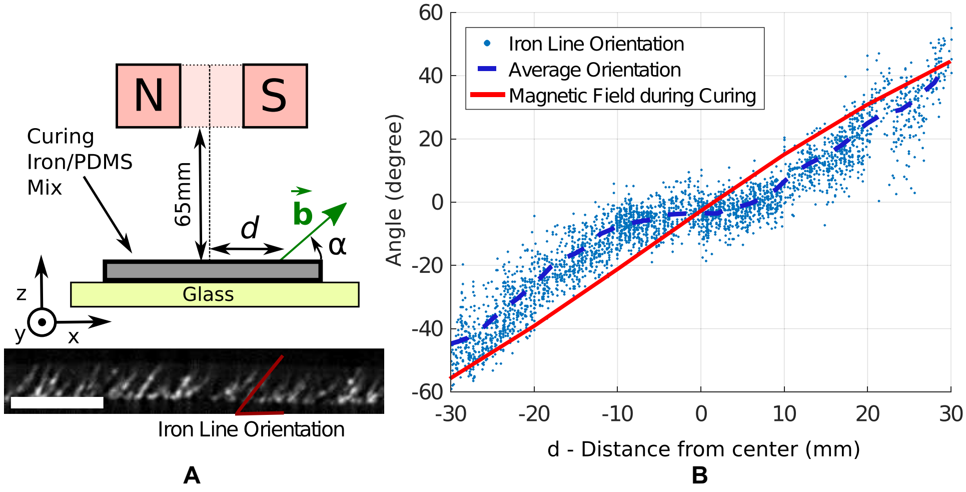

Fig. 3. Iron line orientation inside the PDMS matrix. (**A**) Micro-CT reconstruction of the polymer/iron mix. The iron lines aligned with the magnetic field direction during the polymer curing. (**B**) Iron line direction versus position. The direction of the iron lines followed the curing magnetic field direction.

Supplementary Material D. No snapping effect occurred in the simulation because the interaction between the microrobots and the surface tension interaction were not modeled.

To understand the leading phenomenon of the microrobot snapping, we derived a model of the surface tension–induced force between the microrobots. This calculation, based on a 2D analysis (*31*), gives the order of magnitude of this force, as shown in Supplementary Material E. It particularly shows that the attraction force of the microrobots due to surface tension is of the same order of magnitude as the magnetic field force for a magnet altitude (i.e., distance between the magnet and the water surface) from 10 to 14 mm. For configurations with the magnet at lower altitudes, the magnetic force on the robot is more important. For an altitude at 15 mm, the surface tension force diminished to zero. In this case, the magnetic vertical attraction balanced the microrobot weight, which resulted in no surface deformation. This explains why no snapping was recorded around this value even if the microrobot magnetic trapping force decreased as the distance with the magnet increased. The magnetic interaction between the two microrobots was also simulated using a magnetic dipole model and is presented in Supplementary Material F. It was found to be negligible for every altitude because the direct force of the magnet surpasses it by a factor of at least 500.

The control of a microrobot pair has four DOFs. Two DOFs correspond to the 2D translation of the pattern in the plane defined by the air/water interface. This was controlled by the microscope stage, which moved the water container compared with the magnet's horizontal position. Another DOF corresponds to the rotation of the two microrobots around their mutual center and was controlled by the rotation of the magnet around its axis of symmetry. The last DOF corresponds to the distance between the two microrobots and was controlled by the vertical position of the magnet.

These four controllable inputs were sufficient to perform the manipulation of a floating pattern as shown in Fig. 4B. First, the magnet was lowered to move the microrobots apart and then to position them around the target pattern. Next, the magnet was raised to close the gap between the two microrobots, thus grasping the pattern to allow for subsequent translation and rotation to align with the target fiber substrate. Then, the fiber was raised until it touched the pattern and prevented any relative movement between the pattern and the fiber. The grasping force of the microrobots did not lead to any observable deformation of the pattern.

Last, the magnet was lowered again for the gripper to release the pattern, and the robot pair was moved away. A typical experimental process is recorded and shown in movie S2.

Microrobot force characterization

The magnetization property of the iron/PDMS mixture has been characterized to serve as a general guide for similar microrobot designs. The stiffness of the magnetic trap maintaining the robot on its equilibrium position was measured for this purpose. If we assume that the microrobot magnetic interaction could be represented as a magnetic dipole, the following formulae apply

$$\mathbf{f} = \nabla(\mathbf{m} \cdot \mathbf{b}) \tag{1}$$

$$\mathbf{t} = \mathbf{m} \times \mathbf{b} \tag{2}$$

where $\mathbf{m}$ is the microrobot magnetic moment, $\mathbf{b}$ is the applied magnetic field, $\mathbf{F}$ is the resulting force, and $\mathbf{t}$ is the resulting torque. In ferromagnetic materials, the magnetic moment $\mathbf{m}$ is induced by the magnetic field in a nonlinear way. However, we did not observe any remnant magnetization on the microrobots. Therefore, we modeled the magnetization as a linear function of the magnetic field. This assumption allowed us to describe the magnetization as in a paramagnetic material, which gives the following (*32*)

$$|\mathbf{f}| = \frac{v\chi}{2\mu_0} \nabla \ |\mathbf{b}|^2 \tag{3}$$

where v is the microrobot volume, μ_0 is the vacuum magnetic permeability, and χ is the material magnetic susceptibility. Hence, the magnetic moment amplitude of the microrobot is

$$|\mathbf{m}| = |\mathbf{b}| \frac{v\chi}{2\mu_0} \tag{4}$$

Note that in all considered models in this article, we assumed that the microrobot magnetic moment orientation is given by the magnetic field direction at the curing step. To obtain the microrobot magnetic moment ($\mathbf{m}$) and the material magnetic susceptibility (χ), we measured $\mathbf{f}$ along the south-north axis of the magnet by pressing the microrobot against a glass fiber 86 mm long (corresponding to the height of water in the beaker used in this experiment) with a 120 μm diameter that was perpendicular to the water surface, as sketched in Fig. 5A. The magnet was standing 20 mm above the water surface, and the value of the magnetic field was measured by a gaussmeter with a millimeter resolution. Therefore, we measured the stiffness of the magnetic position control as well as the corresponding magnetic susceptibility calculated using Eq. 3. These results are shown in Fig. 5B. The magnetic susceptibility calculation

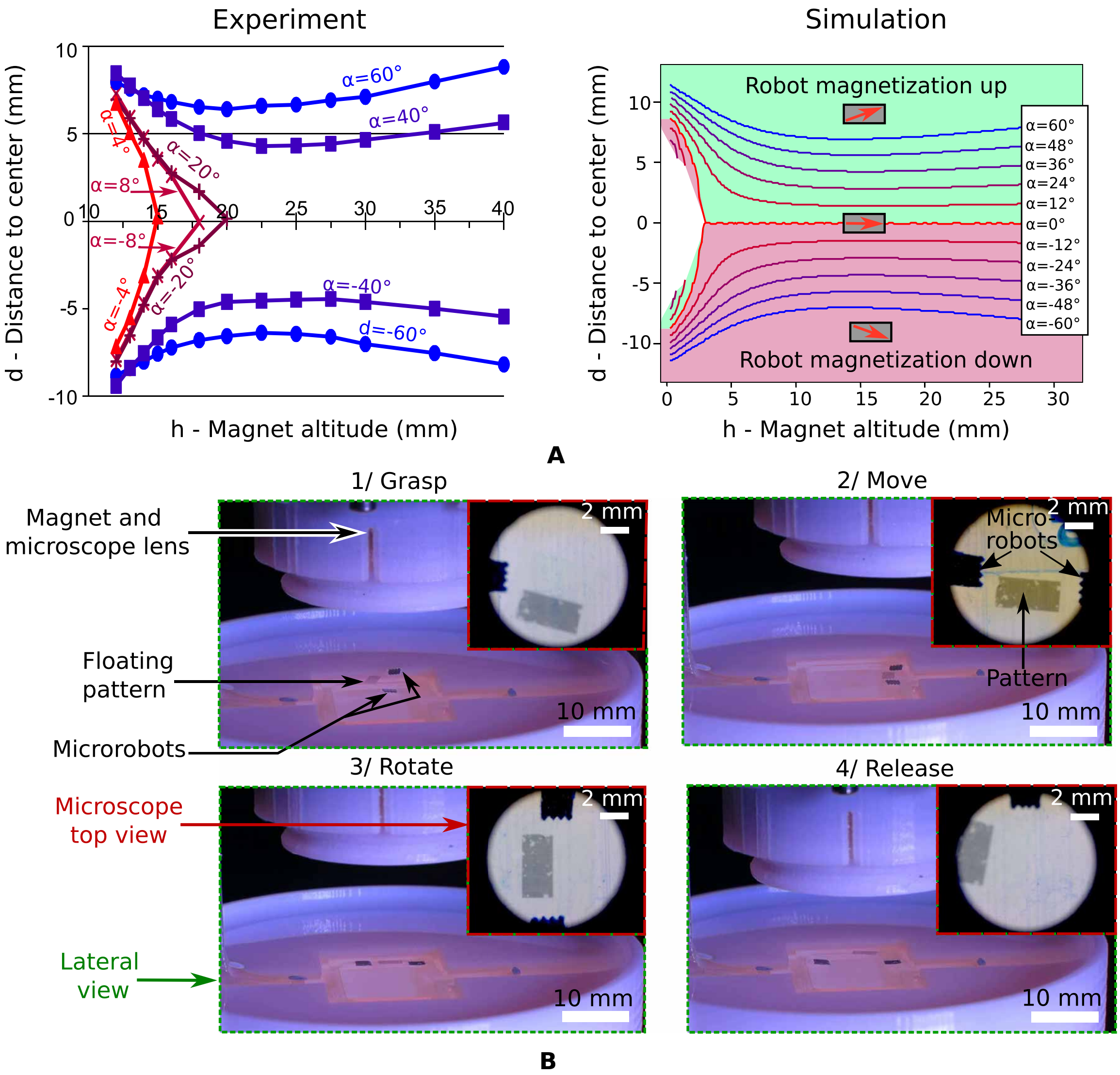

Fig. 4. Magnetic control of the microrobot pair. (**A**) Different equilibrium positions of the microrobot pair as influenced by the vertical position of the magnet. Left: Experimental results. Right: Simulation results acquired using finite element modeling of the magnetic field. (**B**) Optical images showing the microrobot pair manipulating a floating pattern (for animation, see movie S1).

assumed that the microrobot magnetized in the direction of the magnetic field. Therefore, only characterizations for microrobot with $\alpha = 0$ are displayed in Fig. 5B. As α increased, the microrobot force slightly decreased. For $\alpha = 40$, the force decreased 20%, as shown in Supplementary Material G. For the following experiments, which involve the manipulation of wet transfer patterns, we chose microrobots with 20% iron mass, because they exhibit sufficient stiffness and have a low enough magnetization, which reduces the risk of abrupt attraction toward the magnet when placed on the water surface.

To reduce the pattern fluctuation around the steady-state position and to increase transfer accuracy, we used a cover to limit perturbation of the water surface due to airflow during experiments. This reduced the static error from 11 μm to less than 1 μm. Tracking of the pattern's position during steady state is available in Supplementary Material H. The dynamic control of the pattern was fast, and the system reached static equilibrium in less than 3 s for a 500-μm step movement. An overshoot of the control position was observed on the step control (see Supplementary Material H). To determine whether the overshoot is only due to the dynamic of the microrobot, we proposed a model whereby the fluid was assumed to be motionless and that the only forces on the microrobot were those related to the magnetic field and fluid drag. Therefore, at equilibrium, the movement equation is represented as

$$\ddot{x}m + \dot{x}d - \mathrm{x}k = 0 \tag{5}$$

where x is the microrobot relative position to the equilibrium, m is its mass, d is the fluid drag, and k is the magnetic stiffness presented in Fig. 5. To avoid overshoot, the discriminant of the movement equation needs to be positive. Therefore, we can conclude the following criterion on the magnetic stiffness to avoid overshoot

$$k < \frac{d^2}{4m} \tag{6}$$

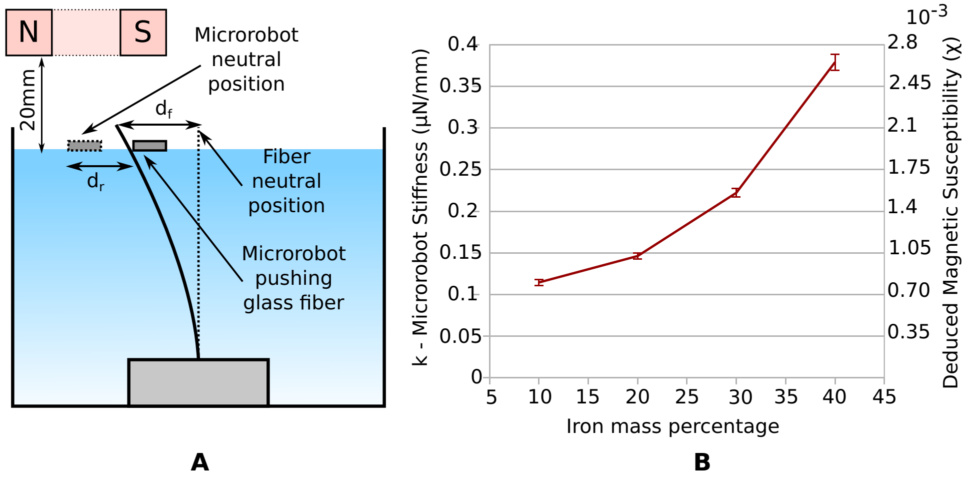

Fig. 5. Force characterization of a single microrobot. (**A**) Schematic illustration of how force characterization was performed. The microrobot pushed a 120-μm-diameter glass fiber; the deformation of the fiber is linked to the applied force. (**B**) Microrobot stiffness versus iron mass concentration with a 20-mm distant magnet. Microrobots with $\alpha = 0$ were characterized. The stiffness was assumed to be linear and 1 mm away from the equilibrium position of the robot. The error bars show the differences between loading and unloading force measurement at 1 mm. By assuming no remnant magnetization, the magnetic susceptibility was also deduced.

By using the proposed microrobot force characterization, the fluid drag can be measured. We refer to Supplementary Material I for details on the experiment. For a 4-mm^2 square microrobot, the measured drag was 4×10^{-6} kg s^{-1}. Therefore, by using Eq. 6, the minimal stiffness that gives rise to an overshoot for a 20% iron mass microrobot is estimated at 7×10^{-3} μN mm^{-1}. In our setup, the stiffness was largely under this value in all the control regions, as shown in Supplementary Material E. Therefore, we can conclude that the overshoot was mainly due to the water movement created by the stage displacement. This overshoot is not a problem for wet transfer applications because we are mainly interested in the position at the steady state. However, for applications where the dynamics of the microrobot are critical, controlling the movement of the magnet rather than the stage would be preferable.

Microrobot-assisted wet transfer

To perform wet transfer of the floating pattern onto an optical fiber, we placed a vertical stage next to the pool with an attached holder extended into the water. This allowed the fiber (or other target structures to be patterned) to be mounted onto the stage and fully immersed in water, enabling subsequent scooping of the floating pattern from below.

The full setup is illustrated in Fig. 6A. Figure 6B presents the fabrication steps to transfer arbitrary Au patterns, such as electrodes or strain gauges, onto a fiber. The steps are as follows:

1) Floating pattern preparation: A polymethyl methacrylate (PMMA) layer with 500-nm thickness was spin-coated on a 50-nm-thick Au device as a scaffold to maintain the pattern's shape during transfer process. The Au and PMMA patterns were subsequently detached from the original substrate, and the pattern was left to float on a water surface.

2) and 3) Microrobot pattern grasping and fiber alignment: Glass optical fibers were cleaned by rubbing with clean room wipe soaked with acetone and isopropanol, respectively. Fibers with diameters of 130, 200, and 830 μm were used as substrates. Oxygen plasma was used for 10 min to remove any remaining organic contamination on the fiber and to increase the hydrophilicity of the surface. This prevented sudden adhesion between the fiber and the pattern during the last transfer steps, which can affect the precision. It also prevented air bubbles sticking to the fiber, which can affect the precision. Note that good pattern adhesion could be achieved without plasma treatment. After cleaning, the fiber was immersed in a tank filled with deionized (DI) water and attached to a holder fixed to a motorized Z stage. Then, the pattern was moved using the microrobots to align with the fiber. Last, the fiber was raised, while maintaining control of the pattern's alignment, until the pattern was in contact with the fiber. After the contact was made, the fiber was raised a further 200 μm above the water's surface to ensure good adhesion between the pattern and the fiber (Fig. 6C).

4) Pattern releasing: The magnet was lowered to release the grasp of the microrobot pair, and the robots were removed. However, the edge of large patterns could still remain attached to the water due to surface tension. This configuration is explained in Supplementary Material J. The fiber was then raised until the pattern fully detached from the water surface. All transfer patterns were left to dry for 10 min in this position.

5) Baking: The fibers with transferred PMMA/Au pattern were left to dry overnight at room temperature. Then, the fibers were baked on a hotplate at 200°C for 1 hour to dehydrate the system to further improve adhesion of the transferred pattern.

6) PMMA dissolving: Last, the PMMA was removed in acetone.

To assess the precision of the transfer process, we measured the shift between two complementary patterns (Fig. 6D). The precision of the overall process was found to be within 5 μm, and the orientation error was below 0.4°. The error was mainly due to residual airflow disturbances not blocked by the cover. Errors also arose due to imperfect alignment of the fiber with respect to the water's surface (i.e., when the fiber is not perfectly parallel with the water's surface). As a result, part of the fiber made contact with the pattern before the rest, leading to a disturbance in pattern control.

In the case of patterns larger than the fiber perimeter, overlap at the bottom side of the fiber could occur, as shown in Supplementary Material J. At this contact location, the long-term adhesion of the pattern was challenging, and it led to a small region of the fiber where reproducible patterning was difficult. This region reduced with increasing diameter of the fiber, starting from about a 90° region on a 130-μm-diameter fiber to a 40° region on an 830-μm-diameter fiber, as shown in Supplementary Material K. This is largely due to the bending of the pattern because of the small radius of curvature on small fibers.

Applications

The precision and the versatility of the proposed microrobot-assisted wet transfer method enabled the fabrication of a variety of devices, as demonstrated by the following examples. For electronic devices, fibers with transferred patterns were clamped on a printed circuit board (PCB), and electrical connections were realized using 25-μm

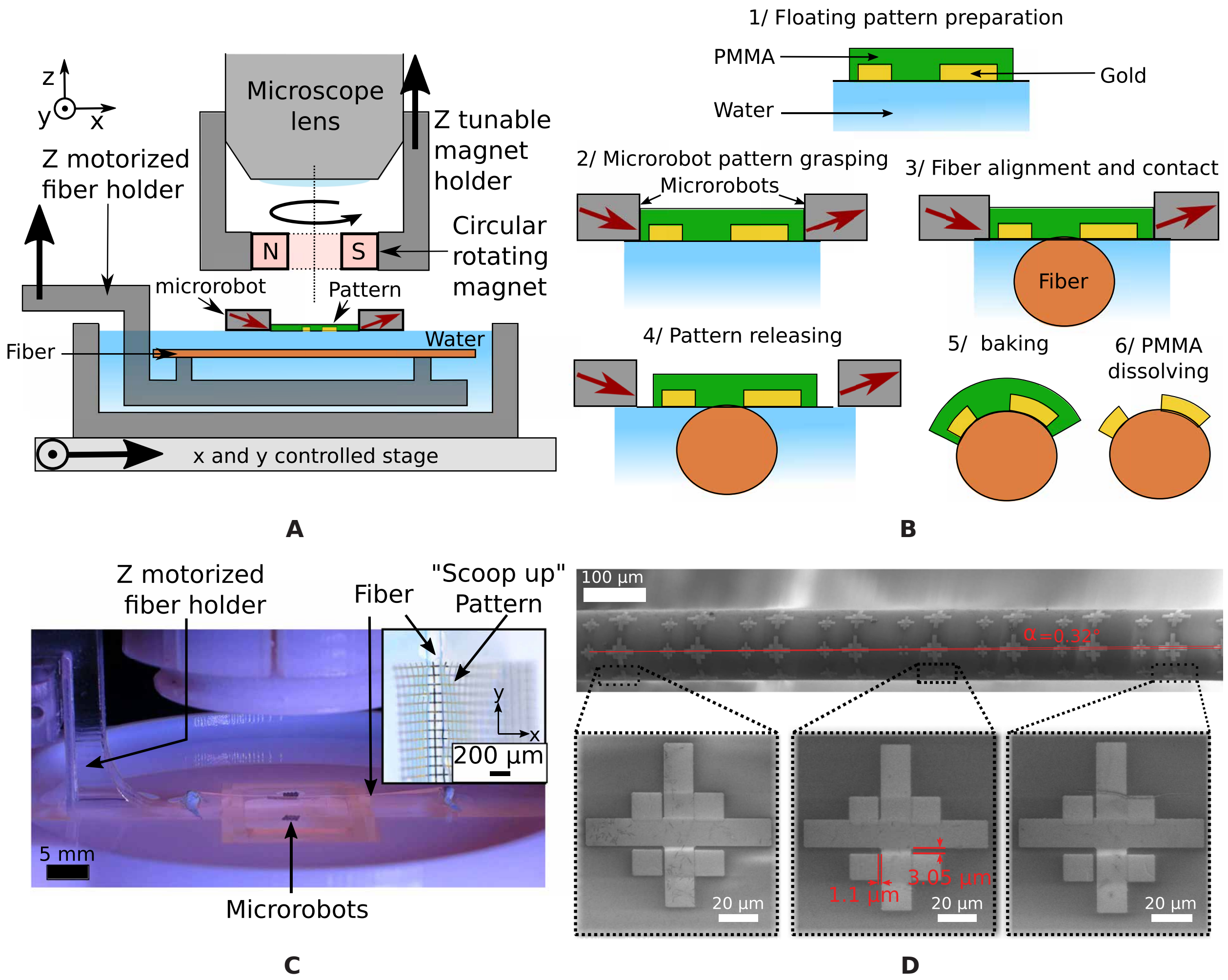

Fig. 6. Fiber patterning using microrobot-assisted wet transfer. (**A**) Side view of the transfer pool with the microrobot pair holding a pattern to be transferred. (**B**) Fabrication workflow for patterning Au microdevices on the fiber using the proposed microrobot-assisted wet transfer. Steps 3 to 6 are recorded in movie S3. (**C**) Floating pattern (grid structures) transferred onto a 200-µm-diameter optical fiber as viewed from the microscope. (**D**) Scanning electron microscopy (SEM) (Tescan SEM/FIB LYRA3 XM) images of two successive transfer position markers for assessing the achievable transfer accuracy of the proposed system.

Au wires to "pin down" the fiber between a pair of PCB bond pads and to connect them with the device electrodes, as shown in Fig. 7A. Last, the fibers were clamped, and the bonding wires were protected using a high-viscosity glob-top epoxy. The connections were tested by using the electrodes as electrochemical sensors. These were realized by electrodepositing Pt black using an external Ag/AgCl reference and Pt counter electrode. Impedance measurements in phosphate-buffered saline solution of the bare electrode and Pt black–covered electrode are presented in Fig. 7A. Such electrochemical sensors can have a range of applications in microcatheters and other implantable devices (*33*).

We further illustrate sequential fabrication comprising several layers of different materials by realizing a two-terminal graphene device on a 200-µm-diameter glass fiber. First, a pair of source-drain Au electrodes was aligned and transferred onto the fiber. This was followed by a precise transfer of graphene flake to bridge the gap between source and drain (Fig. 7B). The integrity of the transferred graphene device was characterized by both Raman spectroscopy and electrical measurements. *I-V* measurements taken before and after an oxygen plasma treatment (to selectively remove graphene) further support the successful fabrication of the graphene device. Graphene serves as a unique electrode material due to its tunable contact properties owing to its finite density of states (*34*). In addition, graphene sheets can be easily functionalized and serve as a platform for label-free biomarker detection (*35*). Further details of the graphene devices are provided in Supplementary Material L.

Active electromechanical devices could also be precisely integrated onto the 3D substrates. A 3-mm-long strain gauge was integrated on a 200-µm-diameter glass fiber and characterized, showing a resistivity of 462.7 ohms with a change of 3 ohms during deformation (see Fig. 7C). We measured the change in resistivity of this gauge as it elongated with the bending of the fiber. The measurements were proven to be reversible, and thus, measurement of fiber's deformation at the location of the patterned strain gauge was possible (see Supplementary Material M). Because this process can be parallelized, 3D orientation reconstruction of a microcatheter at different discrete locations may be developed.

Last, the wet transfer method could be used to pattern on more complex 3D structures. Here, we demonstrate the transfer of an Au pattern on a microtool fabricated using two-photon lithography at

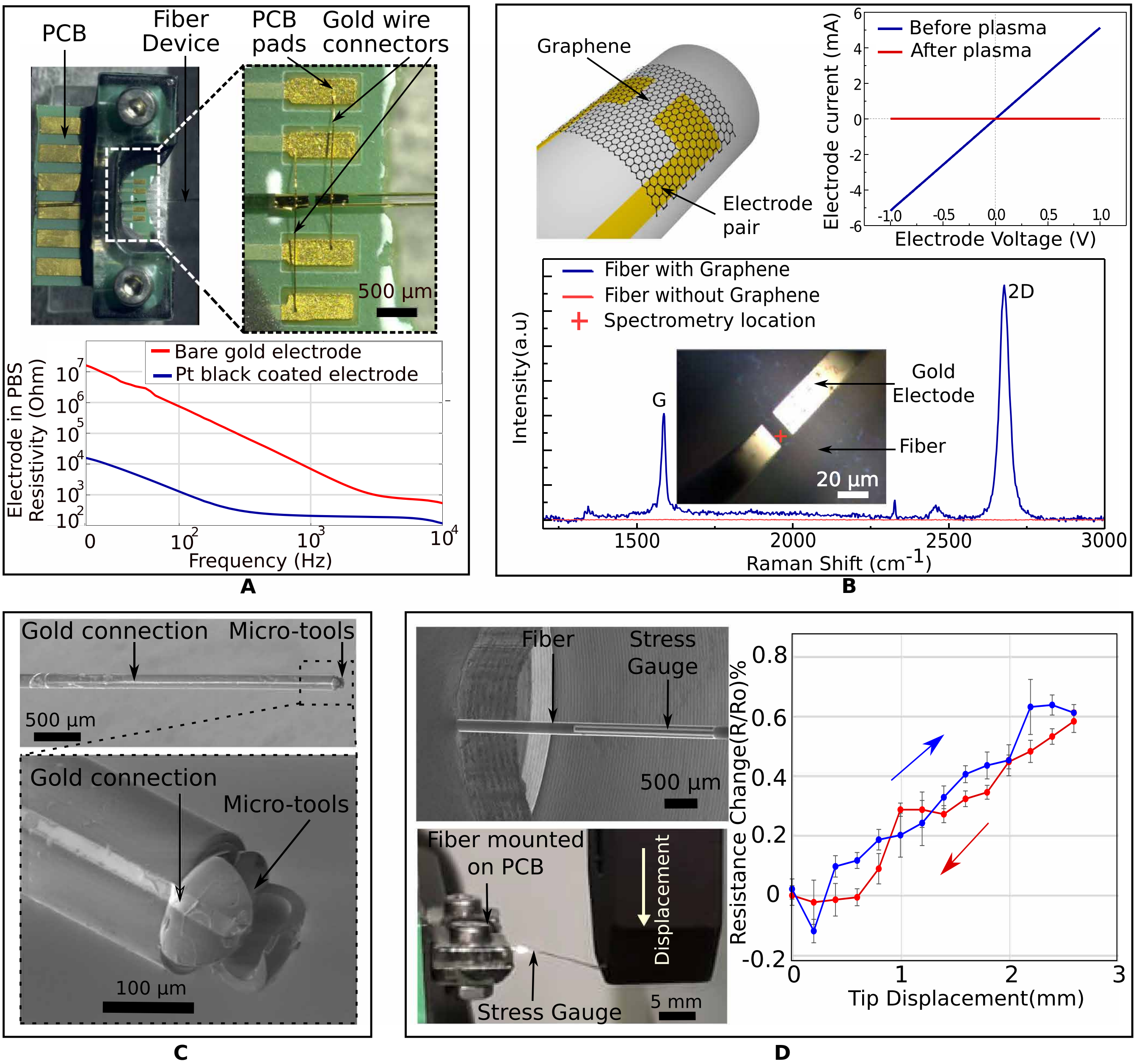

Fig. 7. Example applications of microrobot-assisted wet transfer for fiber functionalization. (**A**) Top: Interface between fiber-supported electrodes and a dedicated PCB. Bottom: Impedance characterization of a two-electrode device with and without electrodeposition of Pt black. (**B**) Fiber-based 2D graphene devices. Sequential wet transfers were made to successively pattern the Au track and then the graphene film. The presence of graphene was assessed with Raman spectrometry and a plasma destructive test. (**C**) SEM picture of a functionalized microtool 3D printed to the tip of a fiber. The Au track was aligned and transferred onto the 3D structure with good conformity. The transfer steps on this microtool are available in movie S4. (**D**) Fiber-based strain gauge designed for measuring fiber deformation based on its resistivity change. SEM picture of the device, picture of the experience, and resulting signal.

the tip of a 170-µm glass capillary fiber (see Fig. 7). The protocol for printing the microtool onto the fiber tip is similar to that described in (*1*) and is described in Supplementary Material M. The pattern could be aligned with the microtool and conformed to the complex 3D surface, paving the way for fabrication of complex electromechanical devices at microscales by using such hybrid microfabrication techniques. A video of the patterning of the gripper is available on movie S4.

DISCUSSION

In this work, we have presented a solution for wet transfer of thin film and 2D crystals with micrometer-level precision on 3D substrates. To achieve this, we developed floating magnetic microrobots capable of storing a preferential magnetization direction. We then manipulated them using equilibrium position under a permanent magnetic field. This allowed for fine-tuning of the obtained robotic microgripper by only adjusting the magnet's position, thus enabling grasp, alignment, and release of floating 2D patterns. The proposed setup is simple, low cost, time efficient, reproducible, and reliable.

To record a preferred magnetization direction of the microrobots, we proposed an easy and low-cost approach based on the fixation of oriented iron powder within a PDMS matrix cured under a magnetic field. We characterized the magnetic susceptibility of this material for different iron concentrations. From Fig. 5, one can note that this curve has neither a nonlinear nor an affine trend. This makes sense because the increase of iron concentration within the PDMS matrix results in longer and more connected lines, thus increasing the level of magnetization. Another interesting point to note is that extrapolation on the current shape would suggest a magnetization for microrobots that contain no iron. Because PDMS is not magnetic, the magnetic susceptibility should undergo a drastic change for values under 10% of iron mass concentration, reaching zero when no iron is present in the material. One hypothesis to explain this would be a sudden increase of the magnetization arising from the formation of iron lines in the matrix when the iron concentration increases over a certain threshold. This can be seen as the magnetic equivalent of the electrical percolation threshold present in materials such as conductive fiber/polymer composites.

The proposed microrobot pair made with this material could perform a wet transfer with a precision below 5 μm. The angle error was below 0.4° by a simple manual rotation of the magnet. The angle error could be further reduced by installing a simple mechanism to control the magnet rotation using regulating screws or a precise step motor.

The micrometer-level precision achieved is necessary for wet transfer onto submillimeter devices and for precise alignment between successive layers. Here, we demonstrated the versatility of the proposed method by fabricating four different types of microdevices. First, we present the fabrication of a single thin-film Au microelectrode and used this for electrochemical sensing. We also showed the capability to create aligned structures by successive transfers of various thin films and 2D crystal by fabricating a two-terminal graphene device with Au electrodes on a 200-μm-diameter glass fiber. We further presented the patterning of a two-terminal Au stress gauge and its capability to measure local fiber deformation. Last, we demonstrate the versatility of this method regarding the substrate via the transfer of an Au electrode on a 3D structure fabricated by two-photon polymerization on the tip of a glass fiber.

Scaling up the proposed setup could encounter some limitations because the surface tension supporting the floating pattern and the microrobot becomes weaker for larger structures. It is generally considered that objects with a dimension greater than the capillary length (2.7 mm in our case) will sink (*36*). However, this limitation is not so important because both the robots and the patterns formed are thin and can be considered as 2D structures with weight scaling only with a power 2 of the dimension. An example of large floating microelectronics has been demonstrated (*12*). Moreover, the magnetic field could be tuned to cancel the robot's weight. As for supporting larger electronic patterns, a thicker PMMA transfer layer could be used to bring the overall density close to water's density.

The proposed method represents a new microfabrication technique for a range of 2D material–based device fabrication onto complex 3D substrates. This opens up new applications in precision surgery and intervention by allowing the design of electrochemical sensors, microactuators, and complex 2D crystal–based electronics devices on submillimetric fiber-based catheters among other applications.

The level of transfer precision as demonstrated by this procedure would also allow for the fabrication of submillimetric devices such as sensor arrays and electronic circuits to perform in situ biomarker detection as well as signal processing. Further work will focus on the fabrication of hierarchical devices based on multilayered van der Waals 2D crystals on nonflat, flexible, and stretchable substrates, as well as integration of active components at a fiber's tip to form a fibrebot that has both actuation and sensing capabilities.

MATERIALS AND METHODS

Microrobot fabrication

The microrobots were made from PDMS mixed with iron powder before curing. The liquid polymer precursor was manually mixed with a curing agent (SYLGARD 184 Silicone Elastomer base and curing agent) and the iron powder (Sigma-Aldrich, 209309-500G, maximum particle size of 44 μm). The mixture was then spin-coated for 1 min at 12 rps on a glass petri dish, resulting in layers with a height of 200 μm.

The glass petri dish was placed in an oven at 90°C for 1 hour, with the magnet placed 65 mm above its center. This corresponds to a magnetic field magnitude of around 8 mT, which is sufficient to orient the particles into lines but lower than a value needed to store significant remnant magnetization. The north and south poles of the magnet were aligned horizontally (i.e., parallel to the petri dish surface). A diametrically magnetized, circular neodymium ring with a 30-mm outer diameter, 10-mm inner diameter, and 10-mm height was used. To avoid interference with the magnetic field during curing, we made the support for the magnet from glass.

After curing, the iron/PDMS layer was peeled from the glass. This layer was then cut with a custom-made graduated cutter to form the different microrobots. Each position corresponded to different iron line directions and, therefore, different preferred magnetization directions.

Microrobot force characterization

The position of the reference frame, the microrobot, and the tip of the fiber were recorded through the microscope and tracked using an OpenCV-based custom software. Experimental views are available in Supplementary Material G. The optical fiber protective polymer cladding was removed (FG200LEA, Thorlab). The fiber stiffness was characterized using a commercial force sensor (FEMTO tool FT-S100000 Microforce Sensing Probe) and exhibited linear behavior in the used region with a measured stiffness of 2.373 μN mm^{-1}. The stiffness of microrobots with four different iron mass concentrations was determined by using the force applied on the fiber at 1 mm away from the equilibrium position. The magnetic susceptibility was derived using the value of the magnetic field and magnetic field gradient at the equilibrium position. This is justified because the force exhibited a linear behavior with the distance to the equilibrium in this region, as shown on Supplementary Material G.

Microrobot structure characterization

The microrobot internal microstructure was studied using x-ray microtomography (Bruker MicroCT Skyscanner 1272). The pixel size of the image was 7.4 μm, and the rotation step was 0.15°. The obtained dataset was then treated on FIJI. To obtain the preferential iron line orientation across the iron/PDMS layer, a 2-mm band was extracted and cut in six equal parts. The images set was then treated and rearranged to increase the contrast of the iron line by combining

10 pictures along the x axis. The plugin OrientationJ Vector Field (*29*) was then used to determine the orientation across the x and y axes.

Wet transfer pattern preparation

In the following, we provide more details on the fabrication steps to obtain the floating device pattern for the wet transfer. Those details expand step 1 of Fig. 6B.

Device fabrication: To prepare the substrates for lithography patterning, Si chips (285-nm SiO_2 layer) were cleaned in an ultrasonic bath with warm acetone and isopropanol, prebaked at 115°C for 1 min, and cleaned in an oxygen plasma etcher (Diener Electronic GmbH + Co. KG) for 5 min. Positive photoresist S1805 (MicroChem) was used for lithography patterning, spin-coated on a Si substrate at 3000 rpm for 30 s, and soft-baked at 115°C for 1 min. The spin-coated substrates were then exposed using the mask aligner (SUSS MicroTec) for 5 s with a 350-W Hg lamp. The exposed samples were then developed in a 351 Developer (Microposit):DI water solution (1:4) for 8 s and flushed with DI water for 30 to 60 s. Au (50 nm) was deposited using e-beam evaporation with the HEX Modular Deposition System (Korvus Technology). Liftoff was carried out using Remover 1165 (MicroChem) for 15 to 30 min under 60°C.

PMMA coating: To prepare the free-standing film for wet transfer, the Si chips with Au-deposited patterns were spin-coated with a layer of PMMA (MicroChem, 495K A8) at 3000 rpm for 1 min.

Si/SiO_2 etching: The pattern was released from the substrate by using a KOH (Sigma-Aldrich) 1 M aqueous solution at 60°C. This resulted in a free-standing PMMA/Au pattern film. The floating film was then transferred to DI water three times and left floating.

SUPPLEMENTARY MATERIALS

robotics.sciencemag.org/cgi/content/full/4/34/eaax8336/DC1
Text
Fig. S1. Magnet magnetic field measurement.
Fig. S2. Schematics of the microrobot cutter.
Fig. S3. Water surface deformation due to the microrobot.
Fig. S4. Clamping hysteresis for thick microrobot.
Fig. S5. Simulation of the magnetic horizontal force on the floating.
Fig. S6. Stable robot position simulation using the measured magnetic field from the magnet.
Fig. S7. Comparison between magnetic force and surface tension force.
Fig. S8. Evolution of the lateral magnetic force over surface tension force (γ) with magnet altitude.
Fig. S9. Microrobot force characterization.
Fig. S10. Position of the pattern grasped by two microrobots at different microscope stage positions.
Fig. S11. Airflow cover impact on precision.
Fig. S12. Microrobot drag force measurement.
Fig. S13. Drying of a pattern on the fiber.
Fig. S14. Transfer on different fiber diameters.
Fig. S15. Raman spectrum of graphene transferred onto fiber at different positions.
References (*37*, *38*)
Movie S1. Summary.
Movie S2. Pattern manipulation.
Movie S3. Transfer example.
Movie S4. Microtool patterning.

REFERENCES AND NOTES

1. M. Power, A. J. Thompson, S. Anastasova, G.-Z. Yang, A monolithic force-sensitive 3D microgripper fabricated on the tip of an optical fiber using 2-photon polymerization. *Small* **14**, 1703964 (2018).
2. J. Paek, I. Cho, J. Kim, Microrobotic tentacles with spiral bending capability based on shape-engineered elastomeric microtubes. *Sci. Rep.* **5**, 10768 (2015).
3. J. Kang, S. Hwang, J. H. Kim, M. H. Kim, J. Ryu, S. J. Seo, B. H. Hong, M. K. Kim, J. B. Choi, Efficient transfer of large-area graphene films onto rigid substrates by hot pressing. *ACS Nano* **6**, 5360–5365 (2012).
4. S. Bae, H. Kim, Y. Lee, X. Xu, J.-S. Park, Y. Zheng, J. Balakrishnan, T. Lei, H. Ri Kim, Y. I. Song, Y.-J. Kim, K. S. Kim, B. Özyilmaz, J.-H. Ahn, B. H. Hong, S. Iijima, Roll-to-roll production of 30-inch graphene films for transparent electrodes. *Nat. Nanotechnol.* **5**, 574–578 (2010).
5. A. Castellanos-Gomez, M. Buscema, R. Molenaar, V. Singh, L. Janssen, H. S. J. van der Zant, G. A. Steele, Deterministic transfer of two-dimensional materials by all-dry viscoelastic stamping. *2D Mater.* **1**, 011002 (2014).
6. L. Wang, I. Meric, P. Y. Huang, Q. Gao, Y. Gao, H. Tran, T. Taniguchi, K. Watanabe, L. M. Campos, D. A. Muller, J. Guo, P. Kim, J. Hone, K. L. Shepard, C. R. Dean, One-dimensional electrical contact to a two-dimensional material. *Science* **342**, 614–617 (2013).
7. A. Reina, X. Jia, J. Ho, D. Nezich, H. Son, V. Bulovic, M. S. Dresselhaus, J. Kong, Large area, few-layer graphene films on arbitrary substrates by chemical vapor deposition. *Nano Lett.* **9**, 30–35 (2008).
8. X. Li, Y. Zhu, W. Cai, M. Borysiak, B. Han, D. Chen, R. D. Piner, L. Colombo, R. S. Ruoff, Transfer of large-area graphene films for high-performance transparent conductive electrodes. *Nano Lett.* **9**, 4359–4363 (2009).
9. J. W. Suk, A. Kitt, C. W. Magnuson, Y. Hao, S. Ahmed, J. An, A. K. Swan, B. B. Goldberg, R. S. Ruoff, Transfer of CVD-grown monolayer graphene onto arbitrary substrates. *ACS Nano* **5**, 6916–6924 (2011).
10. G. F. Schneider, V. E. Calado, H. Zandbergen, L. M. Vandersypen, C. Dekker, Wedging transfer of nanostructures. *Nano Lett.* **10**, 1912–1916 (2010).
11. Y. Fan, K. He, H. Tan, S. Speller, J. H. Warner, Crack-free growth and transfer of continuous monolayer graphene grown on melted copper. *Chem. Mater.* **26**, 4984–4991 (2014).
12. G. A. Salvatore, N. Münzenrieder, T. Kinkeldei, L. Petti, C. Zysset, I. Strebel, L. Büthe, G. Tröster, Wafer-scale design of lightweight and transparent electronics that wraps around hairs. *Nat. Commun.* **5**, 2982 (2014).
13. S. Masubuchi, M. Morimoto, S. Morikawa, M. Onodera, Y. Asakawa, K. Watanabe, T. Taniguchi, T. Machida, Autonomous robotic searching and assembly of two-dimensional crystals to build van der Waals superlattices. *Nat. Commun.* **9**, 1413 (2018).
14. H. Yoo, R. Engelke, S. Carr, S. Fang, K. Zhang, P. Cazeaux, S. H. Sung, R. Hovden, A. W. Tsen, T. Taniguchi, K. Watanabe, G. C. Yi, M. Kim, M. Luskin, E. B. Tadmor, E. Kaxiras, P. Kim, Atomic and electronic reconstruction at the van der Waals interface in twisted bilayer graphene. *Nat. Mater.* **18**, 448–453 (2019).
15. D. Liu, Y. Li, S. Zhao, A. Cao, C. Zhang, Z. Liu, Z. Bian, Z. Liu, C. Huang, Single-layer graphene sheets as counter electrodes for fiber-shaped polymer solar cells. *RSC Adv.* **3**, 13720–13727 (2013).
16. J. Kim, M. Kim, M.-S. Lee, K. Kim, S. Ji, Y.-T. Kim, J. Park, K. Na, K. H. Bae, H. Kyun Kim, F. Bien, C. Young Lee, J.-U. Park, Wearable smart sensor systems integrated on soft contact lenses for wireless ocular diagnostics. *Nat. Commun.* **8**, 14997 (2017).
17. J. Seo, C. Kim, B. S. Ma, T.-I. Lee, J. H. Bong, J. G. Oh, B. J. Cho, T.-S. Kim, Direct graphene transfer and its application to transfer printing using mechanically controlled, large area graphene/copper freestanding layer. *Adv. Funct. Mater.* **28**, 1707102 (2018).
18. S. Tottori, L. Zhang, F. Qiu, K. K. Krawczyk, A. Franco-Obregón, B. J. Nelson, Magnetic helical micromachines: Fabrication, controlled swimming, and cargo transport. *Adv. Mater.* **24**, 811–816 (2012).
19. Z. Ye, E. Diller, M. Sitti, Micro-manipulation using rotational fluid flows induced by remote magnetic micro-manipulators. *J. Appl. Phys.* **112**, 064912 (2012).
20. J. Li, V. V. Singh, S. Sattayasamitsathit, J. Orozco, K. Kaufmann, R. Dong, W. Gao, B. Jurado-Sanchez, Y. Fedorak, J. Wang, Water-Driven micromotors for rapid photocatalytic degradation of biological and chemical warfare agents. *ACS Nano* **8**, 11118–11125 (2014).
21. T. Qiu, S. Palagi, A. G. Mark, K. Melde, F. Adams, P. Fischer, Active acoustic surfaces enable the propulsion of a wireless robot. *Adv. Mater. Interfaces* **4**, 1700933 (2017).
22. M. A. Rahman, N. Takahashi, K. F. Siliga, N. K. Ng, Z. Wang, A. T. Ohta, Vision-assisted micromanipulation using closed-loop actuation of multiple microrobots. *Robotics Biomim.* **4**, 7 (2017).
23. M. Dkhil, A. Bolopion, S. Régnier, M. Gauthier, Modeling and experiments of high speed magnetic micromanipulation at the air/liquid interface, in *2014 IEEE/RSJ International Conference on Intelligent Robots and Systems (IROS 2014)* (IEEE, 2014), pp. 4649–4655.
24. R. T. Mallea, D. Piron, A. Bolopion, P. Lambert, M. Gauthier, Thermocapillary convective flows generated by laser points or patterns: Comparison for the noncontact micromanipulation of particles at the interface. *IEEE Robot. Autom. Lett.* **3**, 3255–3262 (2018).
25. W. Wang, V. Kishore, L. Koens, E. Lauga, M. Sitti, Collectives of spinning mobile microrobots for navigation and object manipulation at the air-water interface, in *2018 IEEE/RSJ International Conference on Intelligent Robots and Systems (IROS)* (IEEE, 2018), pp. 1–9.
26. Y. He, L. Wang, L. Zhong, Y. Liu, W. Rong, Transporting microobjects using a magnetic microrobot at water surfaces, in *2018 15th International Conference on Control, Automation, Robotics and Vision (ICARCV)* (IEEE, 2018), pp. 108–112.
27. E. Diller, J. Zhuang, G. Zhan Lum, M. R. Edwards, M. Sitti, Continuously distributed magnetization profile for millimeter-scale elastomeric undulatory swimming. *Appl. Phys. Lett.* **104**, 174101 (2014).

28. W. Hu, G. Z. Lum, M. Mastrangeli, M. Sitti, Small-scale soft-bodied robot with multimodal locomotion. *Nature* **554**, 81–85 (2018).
29. Z. Püspöki, M. Storath, D. Sage, M. Unser, *Focus on Bio-Image Informatics* (Springer, 2016), pp. 69–93.
30. D. Vella, L. Mahadevan, The "Cheerios effect". *Am. J. Phys.* **73**, 817–825 (2005).
31. E. H. Mansfield, H. R. Sepangi, E. A. Eastwood, Equilibrium and mutual attraction or repulsion of objects supported by surface tension. *Philos. Trans. A Math. Phys. Eng. Sci.* **355**, 869–919 (1997).
32. J. Lipfert, X. Hao, N. H. Dekker, Quantitative modeling and optimization of magnetic tweezers. *Biophys. J.* **96**, 5040–5049 (2009).
33. S. Choi, H. Lee, R. Ghaffari, T. Hyeon, D.-H. Kim, Recent advances in flexible and stretchable bio-electronic devices integrated with nanomaterials. *Adv. Mater.* **28**, 4203–4218 (2016).
34. H. Tan, Y. Fan, Y. Zhou, Q. Chen, W. Xu, J. H. Warner, Ultrathin 2D photodetectors utilizing chemical vapor deposition grown WS_2 with graphene electrodes. *ACS Nano* **10**, 7866–7873 (2016).
35. E. Dubuisson, Z. Yang, K. P. Loh, Optimizing label-free DNA electrical detection on graphene platform. *Anal. Chem.* **83**, 2452–2460 (2011).
36. D. Vella, Floating versus sinking. *Annu. Rev. Fluid Mech.* **47**, 115–135 (2015).
37. J. Zhang, M. Salehizadeh, E. Diller, Parallel pick and place using two independent untethered mobile magnetic microgrippers in *2018 IEEE International Conference on Robotics and Automation* (IEEE, 2018), pp. 123–128.
38. D. Stamou, C. Duschl, D. Johannsmann, Long-range attraction between colloidal spheres at the air-water interface: The consequence of an irregular meniscus. *Phys. Rev. E* **62**, 5263 (2000).

Acknowledgments: We thank B. Li for fruitful discussion on wet transfer and help on floating pattern fabrication, S. Treratanakulchai for the metallic printing of essential tools, F. Deligianni for providing help for the experimental record, P. Kassanos and B. Gil-Rosa for help in PCB designs, and N. Fisher for fruitful discussion on magnetic field simulation. **Funding:** Work was funded by EPSRC grant EP/P012779/1, Micro-Robotics for Surgery (to G.-Z.Y.). **Author contributions:** A.B. proposed and designed the microrobot setup; performed microrobot fabrication, characterization, and modeling; did the transfer experiments; and assisted in the pattern process fabrication. H.T. proposed the wet transfer approach for realizing the fibrebot, developed the device fabrication and floating pattern processes, and characterized the graphene devices. M.P. designed and realized the 3D printing at the fiber tip. F.S. designed and realized the interfacing of the fiber-supported devices, supported A.B. for data acquisition and treatment, designed the robot cutter, and assisted in the pattern fabrication. G.-Z.Y. proposed and designed the fibrebot concept, initiated the project (microrobotics for surgery), secured funding, and supervised all steps of the project. **Competing interests:** The authors declare that they have no competing interests. **Data and materials availability:** All data needed to evaluate the conclusions in the paper are present in the paper and/or the Supplementary Materials.

Submitted 29 April 2019
Accepted 30 August 2019
Published 25 September 2019
10.1126/scirobotics.aax8336

Citation: A. Barbot, H. Tan, M. Power, F. Seichepine, G.-Z. Yang, Floating magnetic microrobots for fiber functionalization. *Sci. Robot.* **4**, eaax8336 (2019).

Science Robotics

Floating magnetic microrobots for fiber functionalization

Antoine Barbot, Haijie Tan, Maura Power, Florent Seichepine, and Guang-Zhong Yang

Sci. Robot. **4** (34), eaax8336. DOI: 10.1126/scirobotics.aax8336

Science Robotics (ISSN 2470-9476) is published by the American Association for the Advancement of Science. 1200 New York Avenue NW, Washington, DC 20005. The title *Science Robotics* is a registered trademark of AAAS.